Recent changes in atmospheric input and primary productivity in the north Indian Ocean

J. Kuttippurath [a,*], S. Maishal [a], P. Anjaneyan [a], N. Sunanda [a], Kunal Chakraborty [b]

[a] CORAL, Indian Institute of Technology Kharagpur, Kharagpur 721302, India
[b] Indian National Centre for Ocean Information Services, Ministry of Earth Sciences, Hyderabad 500090, India

ABSTRACT

Global oceanic regions are rapidly changing in terms of their temperature, oxygen, heat content, salinity and biogeochemistry. Since the biogeochemistry of the oceans is important and pivotal for global food production, and a major part of the world population relies on marine resources for their daily life and livelihood, it is imperative to monitor and find the spatio-temporal changes in the primary productivity of oceans. Here, we estimate the changes in Chlorophyll-a (Chl-a) and Net Primary Productivity (NPP) in the north Indian Ocean (NIO) basins of Bay of Bengal and Arabian Sea for the period 1998–2019. We find a substantial reduction of NPP in NIO since 1998 ($-0.048 \, \text{mg m}^{-3} \, \text{day}^{-1} \, \text{yr}^{-1}$) and the increase in sea surface temperature (SST) ($+0.02 \, ^\circ\text{C yr}^{-1}$) is the primary driver of this change. Furthermore, there is a significant (10–20%) change in the air mass or dust transport to NIO from the period Decade 1 (1998–2008) to Decade 2 (2009–2019). This change in air mass trajectories has also altered NPP in both basins through the changes in nutrient input and associated biogeochemistry. Henceforth, this study cautions the changes in primary productivity of NIO, and suggests regular assessments and continuous monitoring of the physical and biological processes from a perspective of food security and ecosystem dynamics.

1. Introduction

Aerosols and dust play key roles in regulating climate of the Earth through radiative forcing [1]. The aerosols also influence cloud formation, rainfall and air quality [2,3]. In addition, they strongly affect the ocean biogeochemistry and atmospheric composition. Aerosols are transported to different regions of the world and away from their primary source regions. Studies show that the transport of minerals from arid regions influences climate through prevailing wind systems and the mineral deposit over the ocean surface [4].

North Indian Ocean (NIO) is a hotspot of phytoplankton bloom and about 16% of global ocean productivity is contributed by NIO [5]. However, the increasing anthropogenic emissions and global climate change drive declining trends in oceanic primary productivity [6]. NIO, consisting of Bay of Bengal (BoB) and Arabian Sea (AS), is unique and the basins exhibit different physical, chemical and biological characteristics. The nutrient supply to AS is relatively large as desert regions surround it. The seasonal winds bring dust and thus, more nutrients into NIO. These cause sporadic blooms in spring, making AS more productive, which is rare in BoB owing to its higher stratification. Many atmospheric and oceanic processes are closely connected to the Chlorophyll-a (Chl-a) blooms and thus to productivity [7,8]. For example, the wind influences the phytoplankton dynamics in different ways by enhancing their growth, and also suppressing them in the areas of stronger winds. Apart from this, sea salt, dust, mixing and vertical stratification play vital roles in
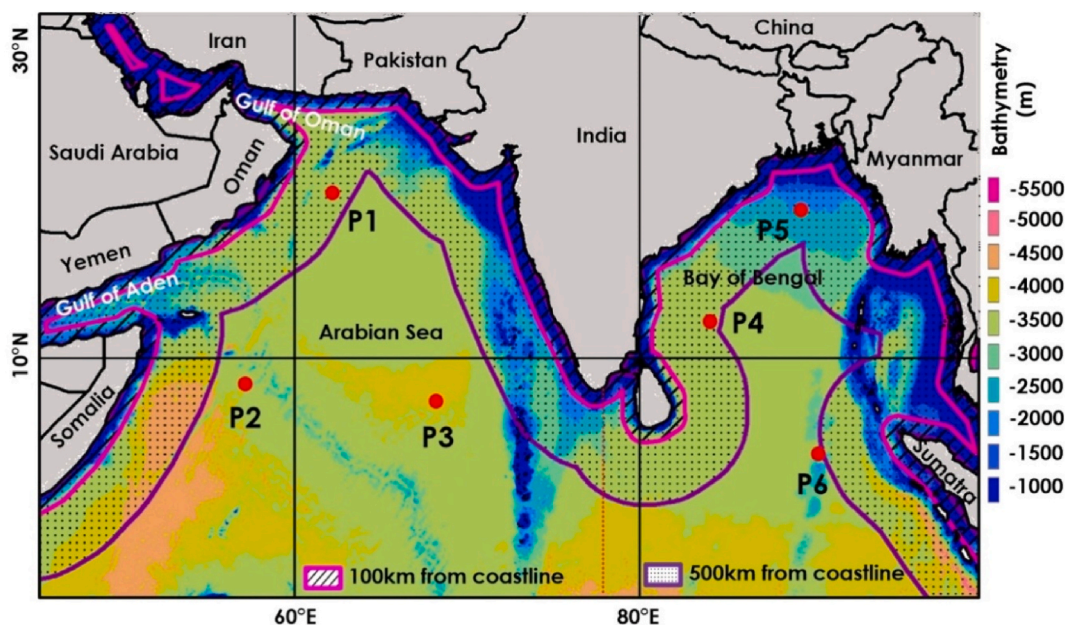

Fig. 1. Bathymetry and specific regions of the north Indian Ocean. The magenta and violet lines mark the extend of 100 and 500 km from the coastline. The points P1–P6 (red dots) show the location selected to find the air mass transport to these regions. (For interpretation of the references to colour in this figure legend, the reader is referred to the Web version of this article.)

regulating the phytoplankton abundance [9]. The coastal and open ocean upwelling also affect the net primary productivity (NPP) [10].

There is substantial dust deposition in NIO, which is second to the north Atlantic [11]. The mineral dust deposition in the global and Indian Oceans has gained significant attention recently. In NIO, dust is transported primarily from the Thar Desert, Middle East and northeast Africa, and is very high during spring and summer [12]. Conversely, dust emission in January–April is restricted to the marine boundary layer and to the low-level continental outflow [13]. The dust over NIO has affected atmospheric heating [14], monsoon rainfall [15] and radiation balance [16]. The southwesterlies during the Indian summer monsoon bring sea-salt aerosols to the land regions [17]. In addition, recent analyses point out the aluminum concentration in the oceans, about $1–6 \text{ g m}^{-2} \text{ yr}^{-1}$ from the south to north BoB [18], which is a proxy for the dust deposition and is higher than that found in AS, Atlantic and Pacific Oceans [19]. Measurements of the vertical distribution of aerosols have also shown high concentrations in the western boundary of BoB [20]. This suggests that the aerosol concentrations vary with altitude and are transported from isolated sources, which are as important as their local sources [14]. The deposition of acidic particles like sulfate or nitrate in the oceans can change their pH. However, the mineral dust iron (Fe), phosphorus (P) and silicate (Si) have decisive roles in the phytoplankton life cycle. The anthropogenic activities are changing the concentration and composition of aerosols, and thus their influence on the oceanic NPP.

For instance, the physical and radiative properties of aerosols are documented as a part of the Indian Ocean Experiment (INDOEX) in 1999 [21]. An earlier study [22] identified southwest monsoon winds and Shamal winds as the potential driving factors for the entrainment of dust into NIO. The Shamal winds from the Mediterranean are strengthened by the orographic effect over Persian Gulf and revoke the moist near-surface winds of the Indian monsoon. These winds can carry vast amounts of dust to AS and precipitate with the Indian monsoon rains [23]. They are present in summer and winter, but the dust loading is primarily tied to the winds in summer [24]. A comprehensive study on the dust deposition in the Indian Ocean suggests that it remains a secondary source in Southern Ocean, and is comparable to the plumes observed in the Atlantic Ocean [18]. The dust transport is also interlinked with the tropical cyclone activity in NIO, which not only alters the trajectories but also promotes the entrainment of dust during the seasons that are not characterised by small wind speeds [25].

The annual variability of Chl-a in a region far from enhanced convective activity could be influenced by dust deposition-induced plankton blooms [26]. An analysis of dust transport and the El Niño Southern Oscillation (ENSO) events over the northwest Indian Ocean finds more dust transport and its input during the La Niña years [27]. A study on the seasonal variability of Chl-a, aerosols, winds and SST using 16 years of satellite data over the Somalia coast showed an enhancement in Chl-a associated with dust deposition in winter in the absence of wind-induced upwelling [28]. Here, we use the space-borne and reanalysis data to study the transport of aerosols and dust, and their impact on the NIO biogeochemistry. Additionally, we have considered trajectory analysis to identify the pathways and potential sources of air mass and their recent changes. We use various statistical methods to examine the seasonal and decadal changes in dust transport, Chl-a and NPP in NIO.
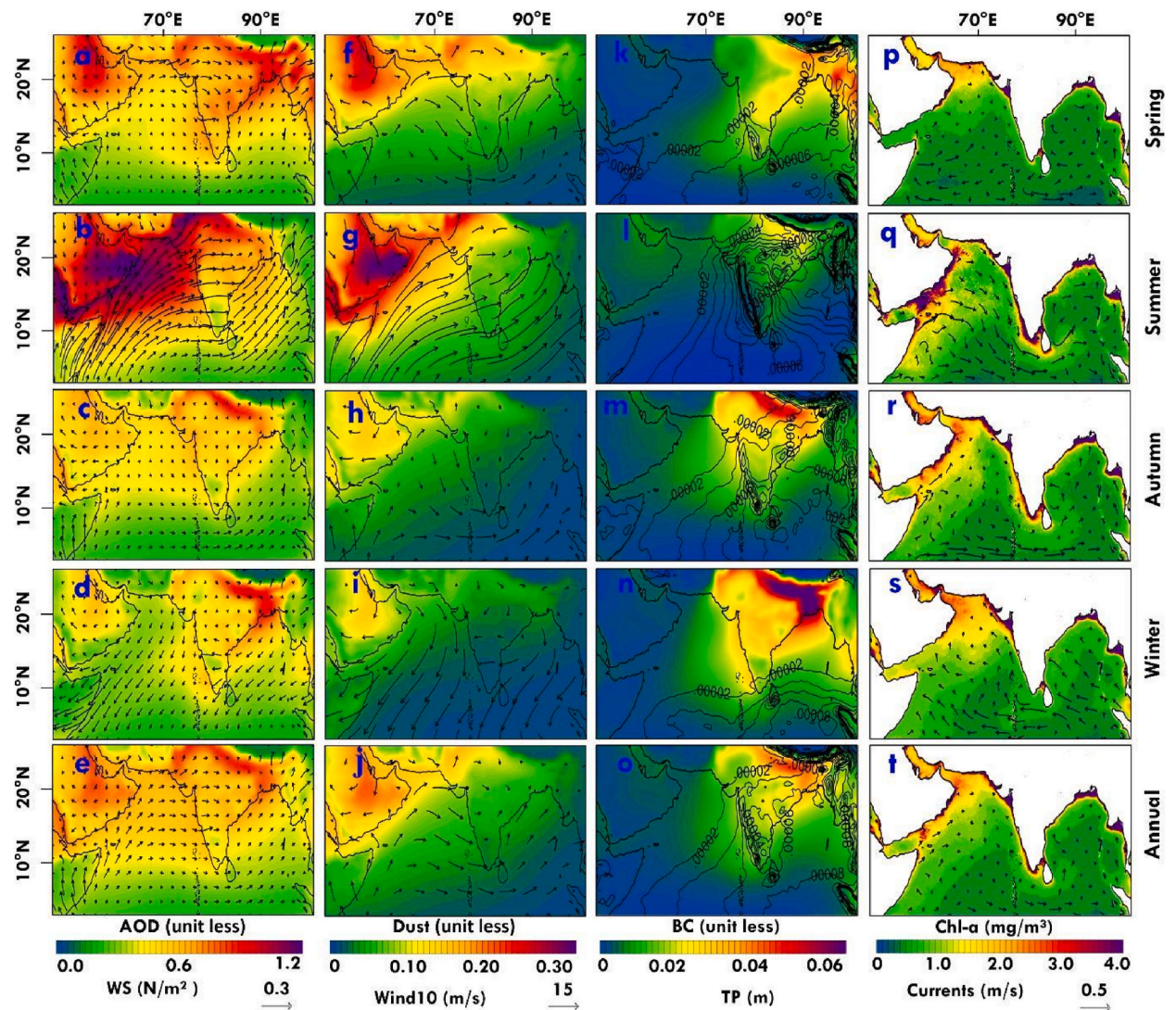
Fig. 2. Seasonal climatology of Aerosol Optical Depth (AOD: a–d), Dust (f–i), Black Carbon (BC: k–n), Chlorophyll-a (Chl-a: p–s) concentration in the north Indian Ocean. Annual climatology of AOD (e), Dust (j), BC (o) and Chl-a (t) are also shown. Wind Stress (WS), wind vectors (10 m), total precipitation (TP) and ocean surface currents for seasonal and annual are overlayed in the respective illustrations. The climatology is calculated for the period 1998–2019.

2. Data and methodology

We have used the Modern-Era Retrospective Analysis for Research and Application version 2 (MERRA-2) Aerosol Optical Depth (AOD) at 550 nm, particulate matter (PM2.5, dust), black carbon (BC) (all are extinction and have no unit), surface winds and total precipitation (TP) for the period 1998–2019 [29]. MERRA-2 has global coverage from 90°N to 90°S and from 180°E to 180°W at a horizontal resolution of 0.5° × 0.625°, and we have used its monthly mean data. The multi-satellite merged long-term Chl-a data from Ocean Colour Climate Change Initiative (OC–CCI) version 6 are considered to examine the primary productivity [30]. The sea surface temperature (SST) is taken from the National Oceanic and Atmospheric Administration (NOAA) 1/4° daily Optimum Interpolation SST (OISST) version 2 data [31]. In addition, Copernicus Marine Environment Monitoring Service (CMEMS) reanalysis are taken to examine NPP (GLOBAL_REANALYSIS_BIO_001_029), sea surface salinity (SSS) and mixed layer depth (MLD) changes (GLOBAL_-REANALYSIS_PHY_001_031). These global data (90°N–90°S and 180°E–180°W) are available in 0.25° resolution at 75 depth levels for the period 1993–2019. The surface currents data are taken from Ocean Surface Current Analysis Real-time (OSCAR) [32]. These weekly frequency data cover the globe from 80°N to 80°S and from 180°E to 180°W at 0.33° horizontal resolution. The seasonal and annual climatology of Chl-a, AOD, dust, wind, total precipitation and surface currents for both basins (AS and BoB) for the past decades (1998–2008, 2009–2018 and 1998–2019) are computed. The seasons are taken as Spring: March–May, Summer: June–August, Autumn: September–November and Winter: December–February. To ensure consistency in spatial resolution, both Chl-a and

particulate data are mapped to a grid size of $0.5° \times 0.625°$. Although NPP is discussed, most analyses are based on Chl-a as it is a good proxy for the oceanic primary productivity. The linear cross-correlation and long-term trend in AOD and dust with Chl-a are also estimated. The National Geophysical Data Centre (NGDC) ETOPO5 bathymetry data are used for the buffer calculation from the coastline [33]. The bathymetry and features of NIO, including AS and BoB, are shown in Fig. 1.

2.1. HySPLIT trajectory calculation

The Hybrid Single-Particle Lagrangian Integrated Trajectory (HySPLIT) model is considered to calculate air mass transport to determine its origin and source-receptor relationships [34]. To examine the dust deposition in the ocean basins, we have chosen three points in each basin (P1, P2, P3 in AS and P4, P5, P6 in BoB, shown in Fig. 1) with respect to the Chl-a concentrations, and then air mass transport to these selected regions is estimated. The points are selected by applying a correlation analysis such that they represent the highest (P1 in AS and P4 in BoB), modest (P2 in AS and P5 in BoB) and lowest (P3 in AS and P6 in BoB) aerosol regions. The trajectory changes are estimated using the kernel density [35]. The thermodynamic structure of marine boundary layer can change the air mass transport, and Measuring Geographic Distributions (MGD) is calculated using data taken at different altitudes from the Global Data Assimilation System (GODAS) [36].

2.2. Potential source contribution function

Air mass trajectories are generated for the entire study period to estimate the contribution from source regions and to find changes in air mass transport. We use four clusters for each point, which provide a general feature of the main trajectory of air masses. The Kernel Density Estimation (KDE) method is applied to the back trajectories derived from the HySPLIT simulations to find the pattern of air mass reaching the selected points. Trajectories are grouped through the multivariate cluster analysis using the angle distance method defined by the law of cosines [37], to identify the main flow and source region, and to quantify its contribution. The Potential Source Contribution Function (PSCF) is applied to identify the source regions [38]. To calculate PSCF, the whole domain that includes the back trajectory is gridded into i by j array. The PSCF construct can be explained as follows: A trajectory is assumed to collect the material emitted in a cell if its terminus is at the cell at location (i, j). Aerosol can be carried along the trajectory to the receptor site once absorbed into the air parcel. PSCF establishes a probability distribution map that identifies potential source locations for the material responsible for elevated values at the receptor site. If there are m_{ij} points where the measured aerosol parameter exceeds a threshold value chosen for this parameter and there are n_{ij} total endpoints that lie within the cell, the conditional probability, or PSCF, can then be defined as $PSCF_{ij} = \frac{m_{ij}}{n_{ij}}$, here $PSCF_{ij}$ is a conditional probability representing the spatial distribution of likely geographical source locations deduced from the arrival trajectory at the sampling point. Cells associated with high $PSCF_{ij}$ values represent a probable source area. Since $PSCF_{ij}$ is calculated as the ratio of the counts of selected events (m_{ij}) to the counts of all events (n_{ij}), it is likely that relatively small m_{ij} ($\leq n_{ij}$), which are frequently associated with sparse trajectory coverage of the more distant grid cells, will cause $PSCF_{ij}$ to have a high degree of uncertainty in the apparent high value. To remove this trailing effect from PSCF results, we used weighted concentration from the trajectories that crossed the grid cell.

3. Results and discussion

3.1. Distribution of aerosols and Chl-a in NIO

3.1.1. Arabian Sea

Fig. 2 shows the annual averaged and seasonal mean of AOD, dust, BC and Chl-a in AS. The wind stress, winds, TP and ocean currents are also overlaid. The annual averaged distribution of AOD shows high density in the northern AS, particularly north of 14°N (Fig. 2e). The AOD values show about 0.6 in the northern AS, but about 0.2 in the equatorial regions. On the other hand, the high values in dust distribution are more limited to the western coastal regions, between the Gulf of Aden and Gulf of Oman, and is about 0.15 (Fig. 2j). The open ocean waters show about 0.05 or smaller values in the case of dust. Conversely, BC shows the highest values in the Indian coastal regions from south to north, about 0.02–0.03 (Fig. 2o). These analyses suggest that BC and aerosols are more prominent in the eastern side of AS, whereas dust is more in its western side. The increase in dust concentration in the western AS is due to the winds that carry dust from the Arabian and Mediterranean regions.

A strong seasonal cycle of monsoonal winds, currents and precipitation is prominent in AS and thus, significant seasonal changes in dust deposition and Chl-a distribution are expected. In spring, winds do not show any specific pattern as they are mostly northwesterly over AS. In contrast, they are southerly/southwesterly over the western AS (Fig. 2a). The aerosols or dust are transported from the Arabian desert regions, where AOD is about 1.0 and dust is about 0.2. The BC concentrations show higher values in the east India, about 0.03. The distribution of AOD, dust and BC in autumn is very similar to that of spring, but AOD and dust are slightly lower over AS, consistent with the wind pattern and its speed (Fig. 2c, h, m and a, f, k). However, BC concentration is slightly higher than that in spring over the basin. The lowest AOD and dust values are found in winter, in which winds blow from the northeast, where the dust sources are limited (Fig. 2d and i). The AOD and dust concentrations are smaller, but BC levels are higher in winter than in other seasons (Fig. 2n). In addition, BC distribution is mostly confined to the eastern AS and the Indian coastal regions, with values of about 0.03–0.04. The most extensive dust and aerosol depositions over AS are found in summer, in which the winds are southwesterly and are favourable for the transport of dust and aerosols from the Arabian desert regions (Fig. 2b and g). The seasonal highest values of AOD

(1.2) and dust (0.3) are found during this period, and are largest in the northern and western AS. The highest aerosol loading of about 1.0 is found during summer, covering half of the AS basin. As expected, the BC concentrations are the smallest (nearly zero) in summer among all seasons (Fig. 2l). The wet deposition with monsoon rains in June–August makes the lowest concentrations of BC in this season. The lowest aerosol loading over AS is observed in winter, with comparatively higher values of 0.5 in the Arabian Peninsula and southwest coast of India (Fig. 2d).

The upwelling due to strong summer winds is known to enhance NPP in the western AS [39], whereas the mixing due to convection decides the amount of NPP during winter in the northern AS [40]. The largest Chl-a concentration is found in winter, followed by summer (Fig. 2s and q). Nevertheless, the northern AS shows high concentrations in all seasons with smaller spatial and seasonal variability. In summer, the highest Chl-a is observed in the western AS, where the dust deposition is also very large. In other seasons, the deposition of particulates is mainly confined to the coasts of Gulf of Oman or in the northern AS. From the above findings, the role of atmospheric processes on the dust deposition and thus, the Chl-a concentration can be inferred, as the regions with the highest rainfall also have smaller Chl-a concentrations.

3.1.2. Bay of Bengal

In general, the annual averaged AOD shows higher values in the northern BoB (Fig. 2e), where the aerosols are mainly transported from the Indo-Gangetic Plain (IGP). Therefore, IGP and the coastline show the largest values of about 0.4 and its distribution decreases toward the east and southern BoB. The dust also depicts a similar distribution as that of AOD and follows the observed wind patterns there (Fig. 2j). The dust concentrations show the highest values near the western coast, about 0.08. The average BC distribution shows the highest amount in the northern BoB (Fig. 2o).

Interestingly, as for AS, the largest BC concentration is found in winter, about 0.06, which further spreads up to 15°N (Fig. 2n). In spring, the BC concentrations are spread throughout BoB and high values are found parallel to the western coast of BoB (Fig. 2k). The BC concentrations are around 0.03 in the northern BoB, and they are gradually distributed up to 5°N. A similar distribution is also observed in autumn, but is limited mostly to the northern BoB (Fig. 2m).

The highest values of AOD (0.3–0.4) and dust (0.05) are found in summer over BoB, north of 5°N (Fig. 2b and g). The lowest AOD (0.3) and dust concentrations are found in the eastern BoB. The AOD and dust distributions depict a similar spatial pattern in spring and winter, where peak values of about 0.7 for AOD and 0.05 for dust are observed in spring (Fig. 2a, d, f and i). The basin-wide aerosol distribution is absent mainly in autumn, where its distribution is parallel to the land mass along the western BoB (Fig. 2c). As discussed previously for AS, the BC concentrations are just opposite to the distribution of AOD and dust. The BC concentrations are highest in winter (0.06 in the northern BoB), north of 18°N (Fig. 2n). The BC distributions in autumn are higher in the coastal regions, about 0.03, whereas low values of about 0.01 are found above the open ocean regions. BC values above 0.01 are found north of 10°N in spring. Conversely, the summer values of BC are the smallest among the seasons, which could be due to the wet deposition with monsoon rains (Fig. 2l). The annual averaged values of AOD, dust and BC are similar, but are slightly larger than that in autumn as far as their spatial spread is concerned.

The Chl-a concentrations are mostly connected to the distribution of aerosols and dust input into BoB. Typically, the highest Chl–a concentrations are observed near coastal regions, about 0.4–2 mg m^{-3}, as estimated from the annual average (Fig. 2t). The first 100 km from the coast shows the largest values of Chl-a, suggesting the influence of coastal upwelling. Then the following 500 km shows values about 0.2–0.6 mg m^{-3}, beyond which the Chl-a values are minimal in the open waters. As observed in AS, significant seasonal differences are found for Chl-a in the bay. For instance, the peak Chl-a amounts are found in winter (Fig. 2s). Precipitation is very small in winter and it mostly rains south of 10°N during the period. In autumn, the Chl-a concentrations are relatively smaller than that in winter (Fig. 2r).

Similarly, spring also experiences relatively low Chl-a (0.3 mg m^{-3}) in BoB (Fig. 2p). However, in summer, a region of high Chl-a is found, about 0.6 mg m^{-3}, due to upwelling in the southeast AS and the southern Sri Lankan coast and the associated eastward movement by the monsoon currents [41, 42]. The summer and winter Chl-a values are highly influenced by the precipitation, as the southwest and northeast monsoon rains play key roles in the wet deposition of these atmospheric inputs into the ocean (Fig. 2q and s). Except for spring, all seasons show high Chl-a east to Sri Lanka, about 0.5 mg m^{-3}.

3.2. Linkage between atmospheric pollution and Chl–a

3.2.1. Arabian Sea

We examine the correlation between different particulates and Chl-a, an excellent proxy for NPP (Fig. S1 for AS). Since BC does not contribute directly to NPP, we have not considered BC in this correlation analysis. On the other hand, as the deposition of dust and aerosols significantly influence NPP, we have considered both in the analyses and the discussion hereafter. Note that, the aerosols (AOD) also include particulates smaller than 2.5 μm or dust. Yet, we have considered both AOD and dust in the assessment to examine the contribution of particulates together (aerosols or AOD) and the mineral nutrients such as dust. The analyses with annual averaged data show a robust positive correlation north of 12°N, including Gulf of Oman and Gulf of Aden. The correlation is weak and is negative south of 12°N. However, there is a strong seasonal cycle in the Chl-a distribution, as discussed earlier. In spring, a good correlation is found between Chl-a and AOD/dust in almost all regions. In summer, a positive correlation is observed in the eastern coast, Gulf of Aden and Gulf of Oman between Chl-a and AOD or dust. Nevertheless, the correlation is primarily negative and weak in the southern AS. The correlation between Chl-a and AOD or dust is very weak in autumn and winter, around 0.2–0.3, and the positive correlation is restricted to the north-eastern coast of AS due to the northeast winds with limited dust sources. In short, the positive correlation between Chl-a and the particulates are observed mostly in accordance with the direction and strength of winds.
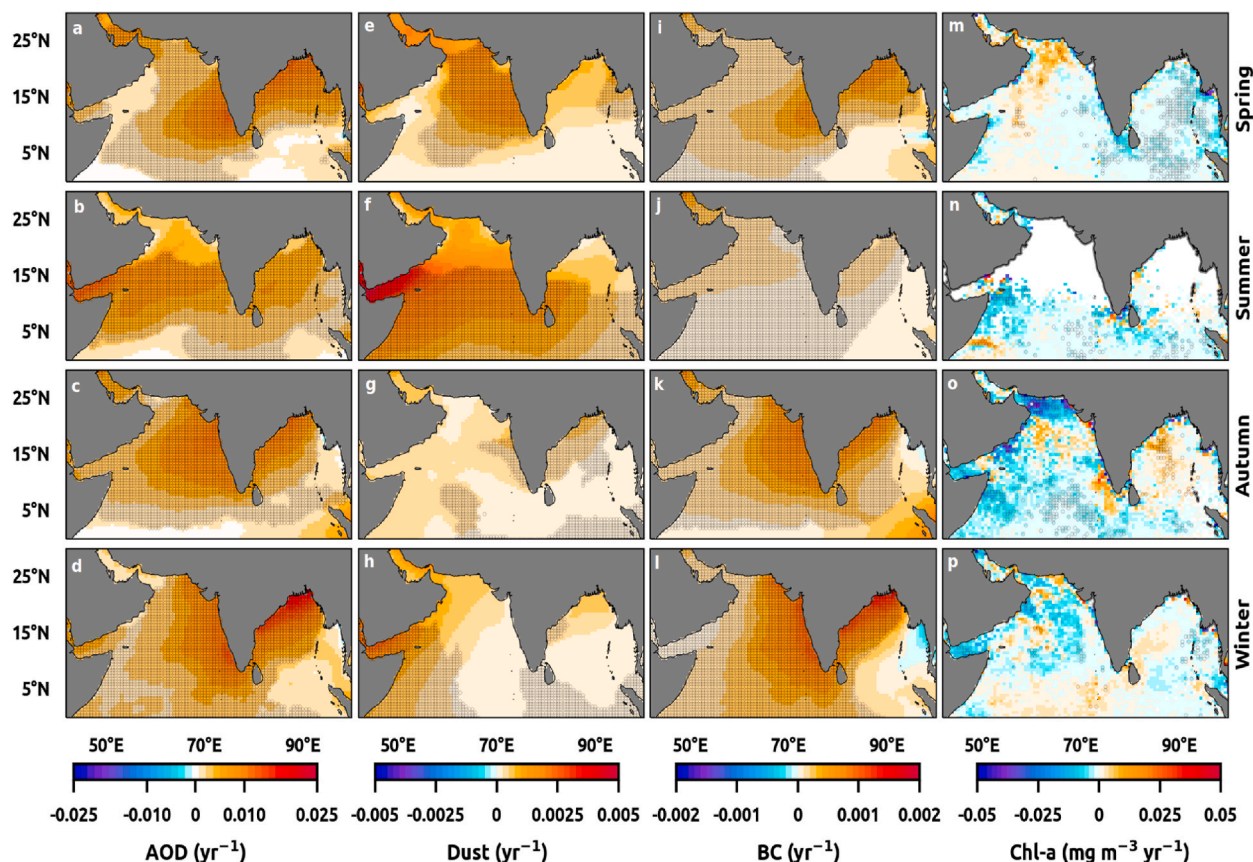
Fig. 3. Seasonal trends of Aerosol optical depth (AOD: a–d), dust (e–h), black carbon (BC: i–l) and Chlorophyll-a (Chl-a: m–p) for the period 1998–2019. The statistically significant trends at the 95% confidence level are hatched.

In winter, a positive correlation is found in Gulf of Aden for AOD and dust, higher than in the eastern AS. This might be due to the winds from the Middle East and Mediterranean regions. The highest positive correlation is observed in spring for AOD and dust, with small areas of negative correlation in the central AS, followed by summer. In this season, a positive correlation is found in the northern AS, but a negative correlation in the southern AS. The overall correlation patterns for autumn and winter are similar for AOD and dust. The annual averaged correlation analyses reveal that the positive correlation is confined north of 12°N. The negative correlation is restricted to the southern AS for AOD and dust.

3.2.2. Bay of Bengal

In BoB (Fig. S2 for BoB), the annual averaged analyses show a high positive correlation in the northern BoB, north of 12°N. The correlation between Chl-a and particulates is negative south of this latitude. Although there are seasonal differences in the correlation between Chl-a and AOD or dust, the general features are similar in all seasons. The positive correlation is found mostly north of 12°N, and in the east and west coasts in all seasons. In spring, the correlation between dust and Chl-a dominates the basin, whereas the influence of AOD is restricted to north of 15°N in terms of the positive correlation. The correlations are very similar in summer, autumn and winter, although the winter shows the highest Chl-a among the seasons. The general correlation pattern shows high positive values in the northern BoB (north of 12°N), where most rivers drain. The correlations are mostly negative north of 10°N. Also, the correlations are negative in the regions of high precipitation and strong northeast winds.

The highest positive correlation is observed for dust in spring. The dust exhibits a positive correlation almost in the entire BoB with small areas of negative correlation in the northeastern BoB. The correlation pattern is similar to that in AS for AOD and dust. Dust dominates the entire basin in spring and autumn seasons, whereas AOD is dominant in the northern BoB, particularly north of 15°N. The annual averaged correlation is similar in the case of AOD and dust, with the highest positive correlation in the northern BoB and negative correlation in the southern BoB.

3.3. Trends in aerosols and Chl-a

3.3.1. Arabian Sea

In AS, all particulates and Chl-a have distinct seasonal cycles and thus, different seasonal trends (Fig. 3a–p). The AOD distribution
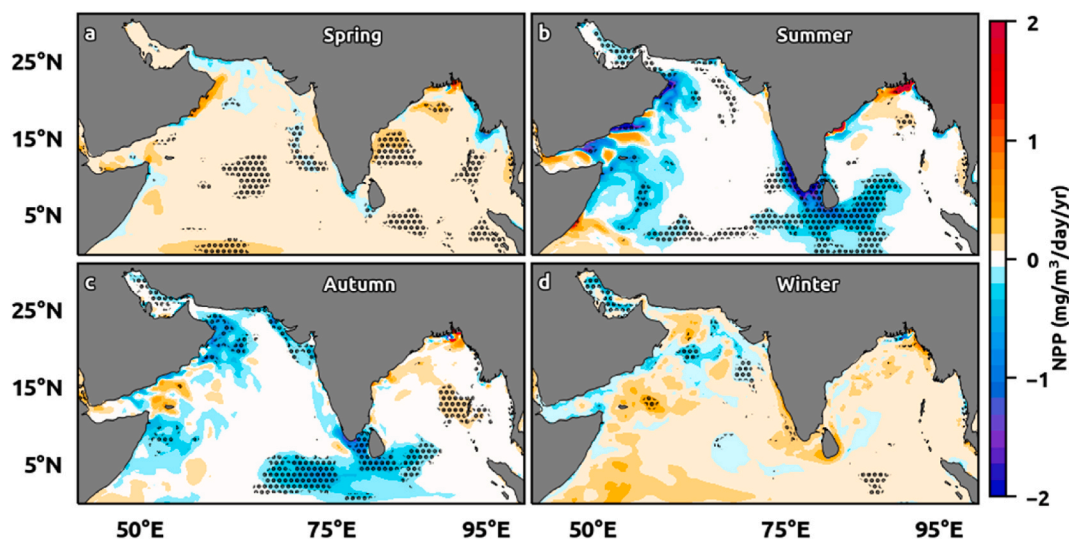
Fig. 4. Seasonal trends in the Net Primary Productivity (NPP) estimated for the period 1998–2019. The statistically significant trends at the 95% confidence level are hatched.

shows significant positive trends across the basin and the largest trends are estimated in the Indian coastal regions, about 0.015 yr^{-1}. The east coast shows the highest and the west coast shows the smallest trends, except in summer (Fig. 3b). The trends in spring, autumn and winter are similar, and are statistically significant (0.004 yr^{-1}) in the west coast (Fig. 3a, c, d). In summer, the AOD trends show significant positive values, between 5° and 17°N, and the basin-wide highest trends (significant) are found over Gulf of Aden (0.02 yr^{-1}). The summer and winter analyses indicate that AOD trends are governed by the air mass transport with the monsoon winds (Fig. 3b and d). Still, the dust deposition in much of the basin is not significant in autumn and winter (Fig. 3g and h). In summer, however, the dust deposition is very high in the entire basin, with a significant positive trend of 0.003 yr^{-1} in Gulf of Aden (Fig. 3f). Positive trends are also found during spring in the east coast and northwest AS, including Persian Gulf and Gulf of Oman, though significant values are observed only in the central and eastern AS (Fig. 3e). The trend values are either zero or insignificant west of 75°E in autumn (Fig. 3g). The BC distribution shows significant positive trends along the east coast and are highest in winter (0.0015 yr^{-1}), followed by autumn (0.001 yr^{-1}), consistent with its seasonal distribution (Fig. 3l and k).

The Chl-a distribution shows insignificant positive trends north of 20°N in spring (Fig. 3m), near the central and south-eastern coast in autumn (Fig. 3o), and comparatively weaker values in the southern and northwest coast in winter (Fig. 3p). However, the trend values in most regions north of 12°N during summer show a gap due to missing values in the data. The analysis shows that spring production is mostly influenced by dust and autumn by all other particulates with AOD.

3.3.2. Bay of Bengal

In BoB, the seasonality is observed in the estimated trends of AOD, dust and thus, in Chl-a (Fig. 3a–p). The trends are higher in the coastal regions, where the aerosols and dust are transported from the land regions, particularly from IGP. The highest significant positive trends in AOD are found in winter (0.02 yr^{-1}) (Fig. 3d), where the winds are from northeast and the continental air mass brings aerosols from these areas. Conversely, the summer trends are smallest among the seasons as the winds are from the relatively pristine oceanic regions (Fig. 3b). The largest trend in dust is found in summer, which implies that most aerosols are particles with less than 2.5 (i.e., dust storms) and are of land origin. The trend values in summer are about 0.002 yr^{-1}, distributed widely over the basin (Fig. 3f). However, the significant values are limited to the south of 15° N. The autumn and winter trends are restricted to the northern BoB and no specific trend is observed elsewhere (Fig. 3g and h). However, the spring trends are positive to the north of 15°N and are about 0.001 yr^{-1}, with significant points only in the eastern region (Fig. 3e). Like AS, winter shows the highest trend (significant) in BC in the northern coast of BoB, around 0.002 yr^{-1} (Fig. 3l). Additionally, a positive trend is observed in autumn and spring with high values along the western coast and in the northern BoB, respectively (Fig. 3k and i).

The highest Chl-a trends are found in autumn in the central BoB, about 0.01 mg m^{-3} yr^{-1} (Fig. 3o). An area of positive trends is also found in the southwest BoB in winter with values of around 0.005–0.01 mg m^{-3} yr^{-1} (Fig. 3p). As found for AS, the analyses reveal that winter trends are dominated by other particulates.

3.3.3. Trends in NPP

Fig. 4 shows the trends of NPP in NIO over the past two decades. In spring, NPP in AS shows a strong positive trend (0.95 mg m^{-3} day^{-1} yr^{-1}) in the coastal Oman apart from the large basin-wide positive values in the central AS and Gulf of Aden, at about 0.2–0.4 mg m^{-3} day^{-1} yr^{-1} (Fig. 4a). The rest of the regions show either slight negative or positive values. In summer, AS shows negative trends (−0.5 mg m^{-3} day^{-1} yr^{-1}) in the upwelling zones in the coastal Somalia, Oman and southwest India, with significant values mostly in the equatorial zones (Fig. 4b). The negative trends in summer, which are confined to the western AS are stronger than those
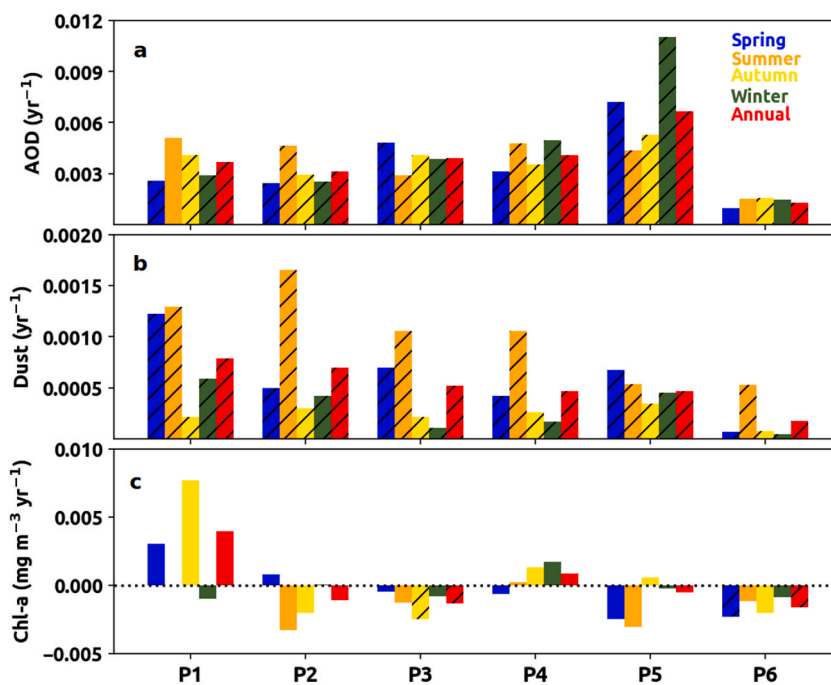
Fig. 5. Annual and seasonal trends in (a) AOD, (b) Dust and (c) Chl-a at the selected points P1, P2, P3, P4, P5 and P6 in the north Indian Ocean for the period 1998–2019. The statistically significant trends at the 95% confidence level are hatched.

in autumn (Fig. 4c). Though most of the western AS exhibit negative trends in summer and autumn, Gulf of Aden and southern Somali coast show positive trends, but are statistically insignificant. The lateral extent of significant negative trend into the southern BoB is in accordance with the decline of NPP in the upwelling zone of southwest India. Nevertheless, the negative trends in the eastern AS remain the same in both seasons, with relatively weaker trends in autumn. Most regions of NIO show a weak insignificant positive trend of about 0.2 mg m^{-3} day^{-1} yr^{-1} during winter and spring (Fig. 4a and d).

3.4. Air mass transport to NIO

3.4.1. Particulates and Chl-a at selected points

The annual AOD concentration at all points shows significant positive trends, which are highest at P5 in winter and spring (significant in both seasons), at about 0.011 yr^{-1} and 0.007 yr^{-1}, respectively, as illustrated in Fig. 5a. The other seasons and points show significant positive trend of about 0.004 yr^{-1}, and the lowest trends are found at P6, at about 0.002 yr^{-1} in all seasons (mostly insignificant). Similarly, dust shows significant positive trends across all seasons and are largest in summer for all points except at P5, suggesting the frequent dust storms during the period (Fig. 5b). The trends in dust are highest and significant in AS at P2 and P1 (0.0018 yr^{-1} and 0.0013 yr^{-1}), followed by P3 and at the BoB point of P4 (0.001 yr^{-1}) because of the outflow from IGP. Therefore, the trends agree with air mass transport from the adjacent desert regions in summer. Spring is the other season showing statistically significant trends and are also highest at P1, at about 0.0012 yr^{-1}, and other selected regional points have significant trends with an average value of 0.0005 yr^{-1}. Conversely, Chl-a exhibits insignificant negative trends in all seasons, except at P1 and P4, where there are positive trends in most seasons (Fig. 5c). The highest positive trend is observed at P1 during autumn, which is insignificant and is about 0.008 mg m^{-3} yr-1, followed by spring with a rate of 0.003 mg m^{-3} yr^{-1}. The analysis at P2, P3, P5 and P6 show negative trends ranging from 0.001 to 0.003 mg m^{-3} yr^{-1} and are mostly statistically insignificant. In general, Chl-a in both oceanic basins are decreasing as discussed before.

3.4.2. Air mass transport pathways and PSCF

As we analyse the contribution of dust and other particulates to oceanic productivity, we examine their local and remote sources. Here, the remote sources are examined with trajectory analyses as the temporal changes in air mass transport would also indicate the difference in aerosol impact on the oceanic regions. In AS, P1 shows air mass origin from the Arabia, in which 90% from the desert regions (Fig. 6a). At P2, the air is transported from the same region, but about 40–50% (Fig. 6b). In contrast, P3 gets most of its air from the east and southwest coast of India, about 40–50% (Fig. 6c). Similarly, the points selected in BoB, e.g., P5, shows the air mass transport from Africa through IGP. The P5 region gets 80–90% of its air from the lower IGP, and P4 gets the rest of the air mass transported through P5 (Fig. 6d and e). Additionally, these points receive air from East Asia, but contributions are small; suggesting similar air mass trajectories and sources for both regions. However, the air mass arriving at P6 is mostly from East Asia through
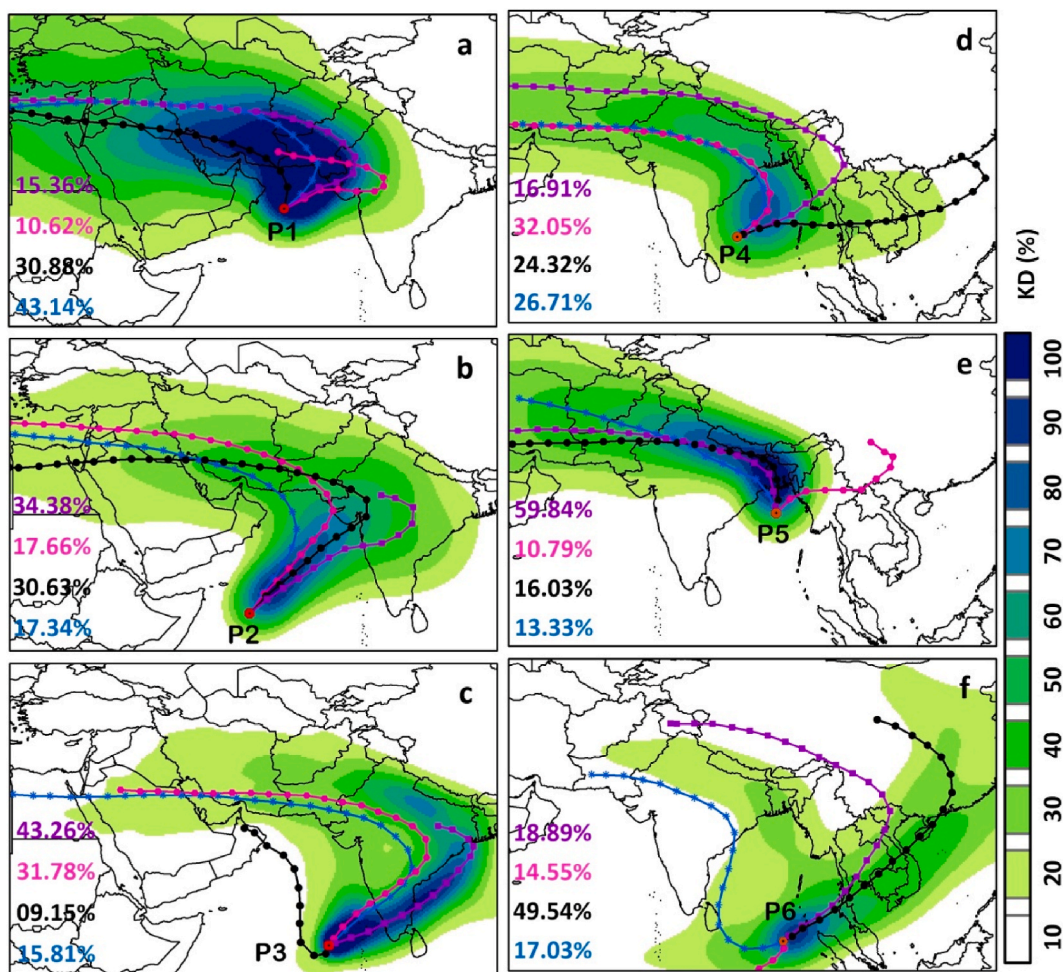
Fig. 6. The air mass transport using kernel density and clustering at the six selected points (a) P1, (b) P2, (c) P3, (d) P4, (e) P5 and (f) P6 averaged for the period 1998–2019.

Southeast Asian countries, about 30–40% (Fig. 6f).

Since there are changes in AOD with seasons, we also checked the air mass transport in different seasons (Fig. S3). In spring, the air mass comes from the African coastal regions to P1 and P2, but it is transported from Australia for P2, about 20–30%. The kernel density is higher at AS for P1, North African coast for P2 and Central AS for P3. In summer, the air mass originates in the south Indian Ocean and is transported through AS to all points. Most air masses come from the northern coastal Africa to P1, near Madagascar to P2 and the southern Indian Ocean to P3. In autumn, the air mass arrives from the Arabian desert to P1, the eastern AS to P2, and is transported from the southern AS and some parts of the Indian land regions to P3. A similar air mass transport is replicated at each point in winter with slightly higher kernel density at P1 and lower density at P2.

In BoB, the air mass transport at P4 and P5 are from the Arabian desert regions and are routed through IGP in autumn and winter. The air masses at P5 are also transported through P4, but some are over the ocean. On the other hand, air mass transport from the eastern Asia through Indonesia is found at P6 in autumn and winter. In spring, the air mass transport to P4 and P5 are from AS through the southern coastal region, but P6 receives most of its air from the Australian region. In summer, the air comes from the southwestern Australia, and P6 receives the air from the northern Australia. In autumn, the air mass comes from Africa and Arabia to P4 and P5, but from the equatorial Indian Ocean and East Asia to P6. The air mass transport in winter also has the same type of trajectories found in autumn for P4 and P5, but from East Asia to P6.

In AS, P1 has the highest probability of the particulates coming from India, Pakistan, Iran and nearby arid and semi-arid regions (Fig. 7a). Conversely, P2 and P3 receive air from the mainland of India, Pakistan and southern Iran (Fig. 7b and c). In BOB for point P4, most particulates come from the northwest India and eastern Pakistan through IGP with the highest potential value (Fig. 7d). However, we observe that IGP acts as a pathway of particulates rather than a source due to the regional morphology. Additionally, point P4 receives particulates from the East Asian countries. The seasonally dry river basin aids in increasing the particulate surge there. Point P5 also has similar sources, but the contribution from Thailand and Laos is negligible. Point P6 receives particulates mainly from China (Fig. 7e and f).
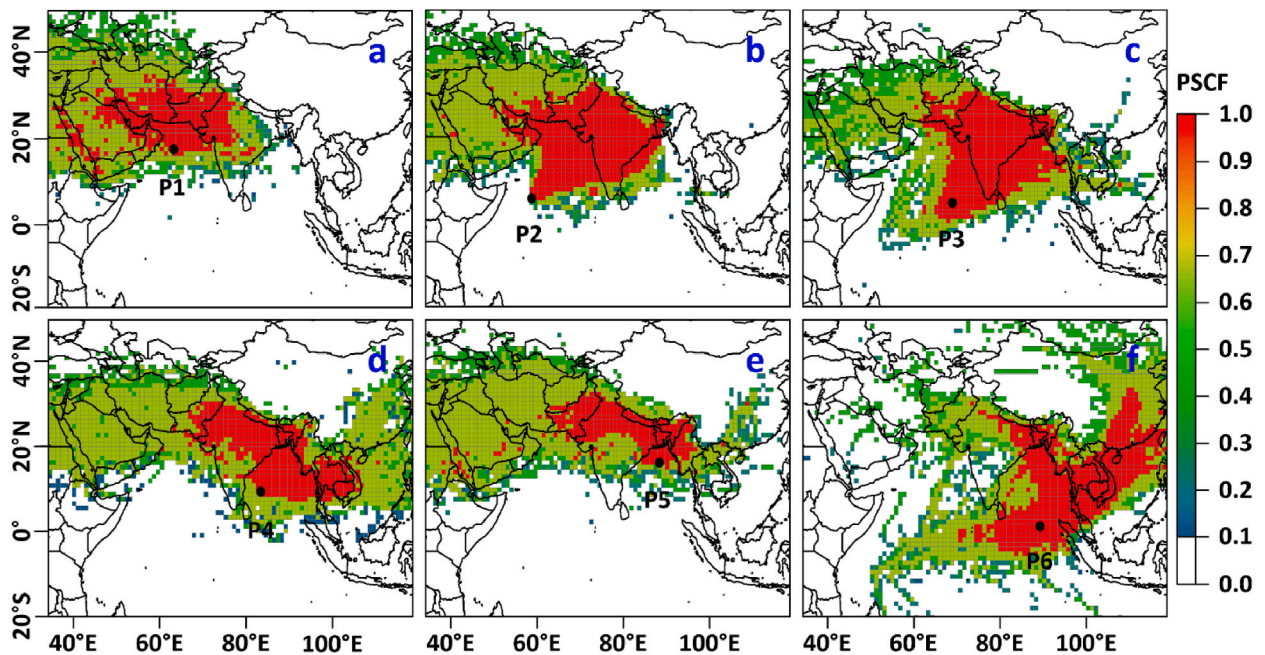
Fig. 7. The potential source contribution function (PSCF) estimated for the selected points (a) P1, (b) P2, (c) P3, (d) P4, (e) P5 and (f) P6 the period 1998–2019.

The air mass trajectory and the source region influence AOD and dust concentration in the selected points. The AOD and dust are highest in P1 for AS and P5 for BoB, located in the northern region of both basins and are influenced by the air mass transport from the Arabian deserts. In addition to this, IGP also contributes dust to P5. The Arabian Peninsula is one of the main dust sources and has peak dust activity in summer [2]. The seasonal distribution (Fig. 1) and trend (Figs. 2 and 5) of dust in AS also show highest values during summer. A similar pattern is observed in BoB during summer; indicating the influence of Arabian deserts in modifying the AOD and dust there. The atmospheric deposition is a source of nutrients like iron, phosphorous and nitrogen [4], which significantly regulate marine productivity. Recent studies have shown the importance of atmospheric deposition in summer and winter monsoon productivity in AS [9]. NPP in AS will be reduced by half in the summer monsoon in the absence of atmospheric iron input via dust deposition [43].

Additionally, dust storms during the winter monsoon can trigger phytoplankton blooms in the central AS, particularly in areas where convective mixing is weak [26]. Since there are no constraints for the atmospheric deposition in AS, particularly from the desert dust, the atmospheric deposition might escalate with the increase in aridity or changes in the winds. The AOD and dust trends in AS are in accordance with this, and favourable changes in the driving forces might make dust deposition to play a prominent role in marine productivity.

3.5. Drivers of Chl-a change

3.5.1. Changes in NPP, SST, SSS and MLD

Fig. 8a–h shows the decadal changes in NPP, SST, SSS and MLD in NIO. Most regions in NIO, particularly in AS, exhibit a decline in NPP during the previous decade D1 (1998–2008) (Fig. 8a). The highest decline is in the summer upwelling regions of the western and eastern AS, with an average value of -2 mg m^{-3} yr^{-1} and is statistically significant. Additionally, the central equatorial region also exhibits a similar trend in NPP in D1. On the other hand, BoB shows a weak trend except along the Indian coastal regions. However, D2 (2009–2019) shows a significant positive trend in AS with high values in the western region (0.5 mg m^{-3} yr^{-1}) (Fig. 8b). Likewise, the positive trend in BoB is mainly confined to the western region. Generally, AS is more productive than BoB due to its intense stratification [44] and the trend distribution follows it, as a higher magnitude in trend is estimated in AS.

In NIO, particularly in AS, marine productivity is adversely affected by the rapid warming at the surface [9,45–47] and in the subsurface [48]. We find that warming in NIO is intense in the central and eastern AS and the southeastern BoB during D1 (Fig. 8c). Warming with an average rate of 0.02 °C yr^{-1} (insignificant) is observed in these regions, where the western AS, including both marginal gulfs, shows a negative trend in SST, with the highest decline of about -0.08 °C yr^{-1} (significant) in Persian Gulf. Contrary to this, the recent decade (D2, 2009–2019) shows intense warming of about 0.02 °C yr^{-1} in NIO (Fig. 8d). This rise in SST in NIO is obvious as both AS (0.029 °C yr^{-1}) and BoB (0.022 °C yr^{-1}) show basin-wide positive SST trends, although cooling is estimated in the northeast AS and at the BoB mouth. However, significant positive trends are mostly found in the central equatorial region. The extremes of NPP trend in AS follow the SST spatial distribution only in the southwest AS and northwest BoB, as both exhibit inverse
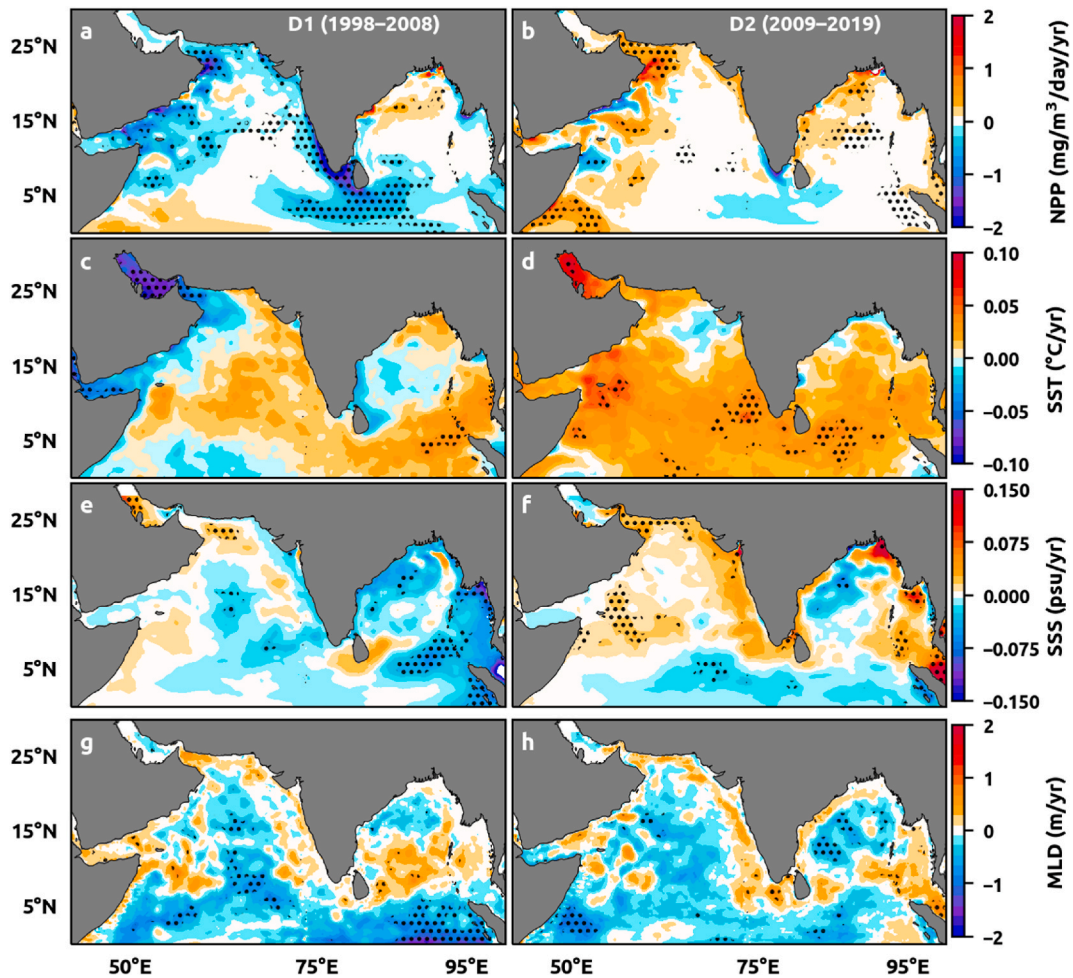
Fig. 8. Trends in Net Primary Productivity (NPP: a–b), Sea Surface Temperature (SST: c–d), Sea Surface Salinity (SSS: e–f) and Mixed Layer Depth (MLD: g–h) in the north Indian Ocean estimated for the periods D1 (1998–2008) and D2 (2009–2019). The statistically significant trends at the 95% confidence level are hatched.

relation during D1. It is noteworthy that, amidst the strong warming in NIO during recent decade, NPP exhibits an increasing trend, which is mostly significant, particularly in the western AS, where warming is profound. Additionally, the central AS shows a weak or no trend during intense warming. Similar variation can be observed for NPP and SST in BoB, with a positive trend in the former in the western bay.

The surface salinity in NIO is governed by evaporation, precipitation, river runoff and surface currents [49]. Excess evaporation over precipitation makes the AS basin high saline than BoB [50], where surplus precipitation over evaporation and high riverine input reduces SSS [51]. The recent decade (D2) shows an increase in salinity in AS and in the coastal regions of BoB, similar to the spatial distribution of positive NPP trend there (Fig. 8f). Though the SSS trend in the open waters of AS is comparatively smaller than the coastal regions, a significant positive trend of 0.01 psu yr^{-1} in these regions can potentially weaken the stratification. This, in turn, will positively affect the vertical mixing and nutrient availability; favouring NPP amidst the warming in the basin. In BoB, an increase in NPP is observed in both decades, which is limited to the northern BoB and the western coastal zones. These regions are highly influenced by Ganga-Brahmaputra riverine system and the decline in salinity is closely related to the riverine inputs there.

The melting of snow in the Himalayan mountains due to the rise in atmospheric temperature [52] might have led to an increase in riverine discharge [53]. The freshwater influx will enhance stratification; thus, contrasting SSS and SST trends are estimated in the northern BoB in both decades (Fig. 8c–f). Additionally, freshwater plays a vital role in BoB by providing essential nutrients to support NPP [54]. The observed decline of SSS in BoB, similar to the positive NPP trend, indicates the possibility of increased nutrient input driven by enhanced river discharge [55]. This influx of nutrients through river discharge might offset the decrease in nutrients caused by reduced vertical mixing due to warming. This suggests that the SST and SSS trends impact the NPP trend.

In summary, the bay experiences freshening at a rate of −0.013 psu yr^{-1}, whereas AS exhibit an increase in SSS of 0.001 psu yr^{-1}, although both are statistically insignificant. The decline in NPP in the western AS during D1, where the mean values are higher during summer (Fig. 2), is of a serious concern. MLD trend shows a decline in the open waters and an increase in the coastal zones, except in
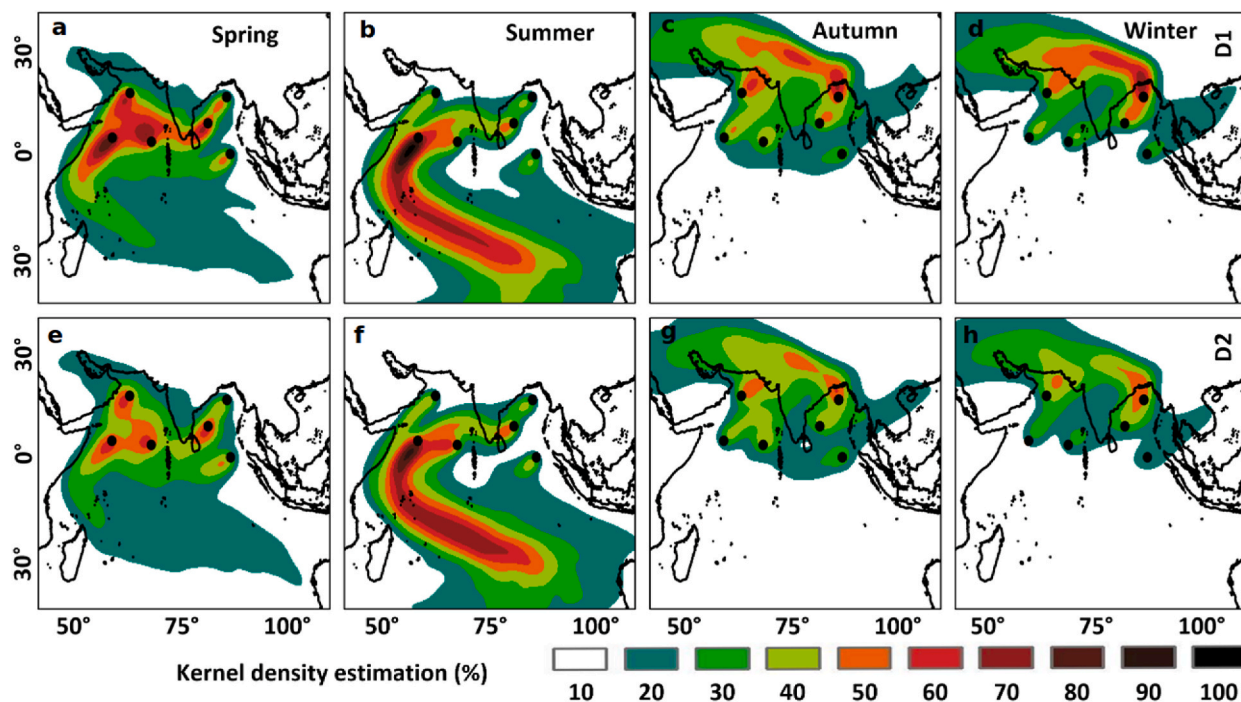
Fig. 9. The seasonal changes in trajectory at the selected points (a) P1, (b) P2, (c) P3, (d) P4, (e) P5 and (f) P6 in the north Indian Ocean for the periods D1 (1998–2008) and D2 (2009–2019).

the southern BoB during both decades. Earlier studies have addressed the decline in NPP in the western AS during summer [50], but increase in the northern AS in winter [7]. Here we observe a strong decadal variation of NPP in NIO with a decline in D1 and an increase in D2. Increased SST can lead to a decrease in NPP since it shows enhanced surface stratification, which in turn inhibits the upward mixing of nutrient-rich subsurface waters. The rise in SSS suggests weak stratification, favouring NPP, particularly in AS during D2. On the other hand, the decline in SSS in BoB conveys an increase in riverine input that causes a positive trend in NPP there. The long-term trend of NPP in NIO shows a significant decline of -0.048 mg m^{-3} day^{-1} yr^{-1}, mainly due to the intense warning $(0.02\,^{\circ}\text{C yr}^{-1})$ in the basin.

3.5.2. Changes in air mass transport

Fig. 9 shows the air mass trajectories for P1, P2 and P3 in AS and P4, P5 and P6 in BoB. The trajectories are shown separately for the past two decades, 1998–2008 (D1) and 2009–2019 (D2). The trajectory density in both decades shows the changes in air mass transport in D2 (2009–2019) from D1 (1998–2008). There is a clear 10% change in trajectory density at each point in the recent decade as compared to the previous decade, as illustrated in Fig. 9a–h. Therefore, the air mass transport is mostly limited to short distances and close to the points in D2 (Fig. 9e–h). In all seasons, the density of air mass transport to all three points is shortened in their transport or distance covered to reach the points. The reduction in transport distance is most obvious at the trajectory tails, as their latitudinal extent is notably reduced.

Since the points are selected with respect to different amounts of Chl-a to represent the diverse nature of primary production in the oceanic region, the air mass trajectory also shows analogous changes, and the most visible change is for P1 followed by P2. The change in trajectory for P3 is also obvious, but is not prominent. This is very clear for all seasons, although the changes in air mass arrival at the point are about 10–20%. Corresponding changes are also found in BoB, as the air masses show marked variations in recent decade for autumn and winter (Fig. 9c–d and g–h). The density changes are mostly within 10–20% for the AS points, and the changes are at the regions near the selected points.

4. Conclusions

A comprehensive analysis on recent changes in dust loading and associated primary production (Chl-a) in NIO is performed. The impact of global warming is found in recent decades and our analyses also suggest changes in the trajectory of air mass transport during the period. We identified three points in the oceanic regions based on the highest, modest and lowest aerosol/dust loading in AS and BoB. The correlation and trend analysis show a strong seasonality, with the highest correlation observed for dust and aerosols in spring and summer over AS and BoB. The distributions of aerosols and dust are highest in spring and summer. Significant changes in air mass transport (about 10% reduction) are also observed in recent decade (2009–2019) with respect to the previous decade, which might be a potential contributing factor for changes in NPP. The SST and SSS also contribute to the changes in Chl-a/NPP and our analyses show a

decline in SSS in BoB of about -0.013 psu yr^{-1}, unlike the positive trend of 0.001 psu yr^{-1} in AS. SST shows a positive trend (0.02 °C yr^{-1}), which is likely to be the main reason for the decrease in NPP (-0.048 mg m^{-3} day^{-1} yr^{-1}) in NIO, although the role of changes in air mass transport and associated nutrients cannot be neglected. However, further studies involving numerical models with biogeo-chemistry are necessary to accurately quantify the contribution of each factor to the NPP/Chl-a change.

Author contribution statement

Jayanarayanan Kuttippurath: Conceived and designed the experiments; Performed the experiments; Analyzed and interpreted the data; Wrote the paper.

S. Maishal, P. Anjaneyan, N. Sunanda, Kunal Chakraborty: Performed the experiments; Analyzed and interpreted the data; Wrote the paper.

Data availability statement

The analysis codes can be provided on request. All data are publicly available and they can also be accessed in their respective sources as listed below. The OC-CCI v6 data was taken from https://www.oceancolour.org/. The MERRA data are available on https://disc.gsfc.nasa.gov. The OSCAR data is available on http://podaac.jpl.nasa.gov/dataset/OSCAR_L4_OC_third-deg. The OISST data are taken from http://apdrc.soest.hawaii.edu/datadoc/oisst.php. The CMEMS reanalysis data are available at https://marine.copernicus.eu/. Etopo5 bathymetry data is taken from https://www.ncei.noaa.gov/products/etopo-global-relief-model.

Funding

Declaration of competing interest

The authors declare that they have no known competing financial interests or personal relationships that could have appeared to influence the work reported in this paper.

Acknowledgements

Appendix A. Supplementary data

Supplementary data to this article can be found online at https://doi.org/10.1016/j.heliyon.2023.e17940.

References

[1] Intergovernmental Panel on Climate Change (IPCC), IPCC Fifth Assessment Report (AR5) Observed Climate Change Impacts Database, Version 2.01. Palisades, NASA Socioeconomic Data and Applications Center (SEDAC), New York, 2017, https://doi.org/10.7927/H4FT8J0X. Accessed 15 January 2022.

[2] J.M. Prospero, P. Ginoux, O. Torres, S.E. Nicholson, T.E. Gill, Environmental characterization of global sources of atmospheric soil dust identified with the nimbus 7 total ozone mapping spectrometer (TOMS) absorbing aerosol product, Rev. Geophys. 40 (1) (2002) 1002, https://doi.org/10.1029/2000RG000095.

[3] J.M. Prospero, F.X. Collard, J. Molinié, A. Jeannot, Characterizing the annual cycle of African dust transport to the Caribbean Basin and South America and its impact on the environment and air quality, Global Biogeochem. Cycles 28 (7) (2014) 757–773, https://doi.org/10.1002/2013GB004802.

[4] T.D. Jickells, Z.S. An, K.K. Andersen, A.R. Baker, et al., Global iron connections between desert dust, ocean biogeochemistry, and climate, Science 308 (2005) 67–71, https://doi.org/10.1126/science.1105959.

[5] G. Kulk, T. Platt, J. Dingle, T. Jackson, B.F. Jönsson, H.A. Bouman, R.J.W. Brewin, M. Doblin, M. Estrada, et al., Primary production, an index of climate change in the ocean: satellite-based estimates over two decades, Rem. Sens. 12 (2020) 826, https://doi.org/10.3390/rs12050826.

[6] M.J. Behrenfeld, R.T. O'Malley, D.A. Siegel, C.R. McClain, J.L. Sarmiento, G.C. Feldman, A.J. Milligan, P.G. Falkowski, R.M. Letelier, E.S. Boss, Climate-driven trends in contemporary ocean productivity, Nature 444 (7120) (2006) 752–755, https://doi.org/10.1038/nature05317.

[7] P. Anjaneyan, J. Kuttippurath, P.V.H. Kumar, S.M. Ali, M. Raman, Spatio-temporal changes of winter and spring phytoplankton blooms in Arabian sea during the period 1997–2020, J. Environ. Manag. 332 (2023), 117435, https://doi.org/10.1016/j.jenvman.2023.117435.

[8] J. Kuttippurath, N. Sunanda, M.V. Martin, K. Chakraborty, Tropical storms trigger phytoplankton blooms in the deserts of north Indian Ocean, npj Clim. Atmos. Sci. 4 (1) (2021) 11. https://doi:10.1038/s41612 -021-00166-x.

[9] N. Sunanda, J. Kuttippurath, R. Peter, K. Chakraborty, A. Chakraborty, The impact of SARS2 COVID-19 lockdown on the primary productivity of north Indian Ocean, Front. Mar. Sci. 8 (2021), 669415. https://doi: 10.3389/fmars.2021.669415.

[10] P.N.M. Vinayachandran, Y. Masumoto, M.J. Roberts, J.A. Huggett, I. Halo, A. Chatterjee, P. Amol, G.V. Gupta, A. Singh, A. Mukherjee, S. Prakash, Reviews and syntheses: physical and biogeochemical processes associated with upwelling in the Indian Ocean, Biogeosciences 18 (22) (2021) 5967–6029, https://doi.org/10.5194/bg-18-5967-2021.

[11] N.M. Mahowald, A.R. Baker, G. Bergametti, N. Brooks, R.A. Duce, T.D. Jickells, N. Kubilay, J.M. Prospero, I. Tegen, Atmospheric global dust cycle and iron inputs to the ocean, Global Biogeochem. Cycles 19 (4) (2005), https://doi.org/10.1029/2004GB002402.

[12] F. Li, V. Ramanathan, Winter to summer monsoon variation of aerosol optical depth over the tropical Indian Ocean, J. Geophys. Res. Atmos. 107 (D16) (2002), https://doi.org/10.1029/2001JD000949. AAC-2.

[13] B. Srinivas, M.M. Sarin, R. Rengarajan, Atmospheric transport of mineral dust from the Indo-Gangetic Plain: temporal variability, acid processing, and iron solubility, G-cubed 15 (8) (2014) 3226–3243, https://doi.org/10.1002/2014GC005395.

[14] S.K. Satheesh, K.K. Moorthy, S.S. Babu, V. Vinoj, C.B.S. Dutt, Climate implications of large warming by elevated aerosol over India, Geophys. Res. Lett. 35 (19) (2008), https://doi.org/10.1029/2008GL034944.

[15] V. Vinoj, P.J. Rasch, H. Wang, J.H. Yoon, P.L. Ma, K. Landu, B. Singh, Short-term modulation of Indian summer monsoon rainfall by West Asian dust, Nat. Geosci. 7 (4) (2014) 308–313, https://doi.org/10.1038/ngeo2107.

[16] S.K. Satheesh, J. Srinivasan, Enhanced aerosol loading over Arabian Sea during the pre-monsoon season: natural or anthropogenic?, 21–1, Geophys. Res. Lett. 29 (18) (2002), https://doi.org/10.1029/2002GL015687.

[17] K.K. Moorthy, S.K. Satheesh, Characteristics of aerosols over a remote island, Minicoy in the Arabian Sea: optical properties and retrieved size characteristics, Q. J. R. Meteorol. Soc. 126 (562) (2000) 81–109, https://doi.org/10.1002/qj.49712656205.

[18] M.M. Grand, C.I. Measures, M. Hatta, W.T. Hiscock, W.M. Landing, P.L. Morton, C.S. Buck, P.M. Barrett, J.A. Resing, Dissolved Fe and Al in the upper 1000 m of the eastern Indian Ocean: a high-resolution transect along 95° E from the Antarctic margin to the Bay of Bengal, Global Biogeochem. Cycles 29 (3) (2015) 375–396, https://doi.org/10.1002/2014GB004920.

[19] N. Mahowald, K. Kohfeld, M. Hansson, Y. Balkanski, S.P. Harrison, I.C. Prentice, M. Schulz, H. Rodhe, Dust sources and deposition during the last glacial maximum and current climate: a comparison of model results with paleodata from ice cores and marine sediments, J. Geophys. Res. Atmos. 104 (D13) (1999) 15895–15916, https://doi.org/10.1029/1999JD900084.

[20] V. Sreekanth, P. Kulkarni, Spatio-temporal variations in columnar aerosol optical properties over Bay of Bengal: signatures of elevated dust, Atmos. Environ. 69 (2013) 249–257, https://doi.org/10.1016/j.atmosenv.2012.12.031.

[21] V. Ramanathan, P.J. Crutzen, J. elieveld, A.P. Mitra, et al., Indian Ocean experiment: an integrated analysis of climate forcing and effects of the great Indo–Asian haze, J. Geophys. Res. 106 (2001) 28371–28398, https://doi.org/10.1029/2001JD900133.

[22] K.W. Glennie, A.K. Singhvi, Event stratigraphy, paleoenvironment and chronology of SE Arabian deserts, Quat. Sci. Rev. 21 (7) (2002) 853–869, https://doi.org/10.1016/S0277-3791(01)00133-0.

[23] V. Ramaswamy, P.M. Muraleedharan, C.P. Babu, Mid-troposphere transport of Middle-East dust over the Arabian Sea and its effect on rainwater composition and sensitive ecosystems over India, Sci. Rep. 7 (1) (2017), 13676, https://doi.org/10.1038/s41598-017-13652-1.

[24] Y. Yu, M. Notaro, Z. Liu, F. Wang, F. Alkolibi, E. Fadda, F. Bakhrjy, Climatic controls on the interannual to decadal variability in Saudi Arabian dust activity: toward the development of a seasonal dust prediction model, J. Geophys. Res. Atmos. 120 (5) (2015) 1739–1758, https://doi.org/10.1002/2014JD022611.

[25] V. Ramaswamy, Influence of tropical storms in the northern Indian ocean on dust entrainment and long-range transport, 40, in: D. Tang, G. Sui (Eds.), Typhoon Impact and Crisis Management. Advances in Natural and Technological Hazards Research, Springer, Berlin, Heidelberg, 2014, pp. 149–174, https://doi.org/10.1007/978-3-642-40695-9_7.

[26] P. Banerjee, S. Prasanna Kumar, Dust-induced episodic phytoplankton blooms in the Arabian Sea during winter monsoon, J. Geophys. Res. Oceans 119 (10) (2014) 7123–7138, https://doi.org/10.1002/2014JC010304.

[27] P. Banerjee, S. Prasanna Kumar, ENSO modulation of interannual variability of dust aerosols over the northwest Indian Ocean, J. Clim. 29 (4) (2016) 1287–1303, https://doi.org/10.1175/JCLI-D-15-0039.1.

[28] M. Shafeeque, S. Sathyendranath, G. George, A.N. Balchand, T. Platt, Comparison of seasonal cycles of phytoplankton chlorophyll, aerosols, winds and sea-surface temperature off Somalia, Front. Mar. Sci. 4 (2017) 386, https://doi.org/10.3389/fmars.2017.00386.

[29] Global Modeling and Assimilation Office (GMAO) (2015), MERRA-2 instM_2d_gas_Nx: 2d, Monthly Mean, Instantaneous, Single-Level, Assimilation, Aerosol Optical Depth Analysis V5.12.4, Greenbelt, MD, USA, Goddard Earth Sciences Data and Information Services Center (GES DISC), Accessed: 28.04.2023, 10.5067/XOGNBQEPLUC5.

[30] S. Sathyendranath, R.J. Brewin, C. Brockmann, V. Brotas, B. Calton, A. Chuprin, P. Cipollini, A.B. Couto, J. Dingle, R. Doerffer, C. Donlon, An ocean-colour time series for use in climate studies: the experience of the ocean-colour climate change initiative (OC-CCI), Sensors 19 (19) (2019) 4285, https://doi.org/10.3390/s19194285.

[31] B. Huang, C. Liu, V. Banzon, E. Freeman, G. Graham, B. Hankins, T. Smith, H.-M. Zhang, Improvements of the daily Optimum interpolation Sea Surface temperature (DOISST) version 2.1, J. Clim. 34 (2021) 2923–2939, https://doi.org/10.1175/JCLI-D-20-0166.1.

[32] F. Bonjean, G.S. Lagerloef, Diagnostic model and analysis of the surface currents in the tropical Pacific Ocean, J. Phys. Oceanogr. 32 (10) (2002) 2938–2954, https://doi.org/10.1175/1520-0485(2002)032<2938:DMAAOT>2.0.CO;2.

[33] National Geophysical Data Center, 5-minute Gridded Global Relief Data (ETOPO5), National Geophysical Data Center, NOAA, 1993, https://doi.org/10.7289/V5D798BF [access date: 22.11.2022].

[34] A.F. Stein, R.R. Draxler, G.D. Rolph, B.J. Stunder, M.D. Cohen, F. Ngan, NOAA's HYSPLIT atmospheric transport and dispersion modeling system, Bull. Am. Meteorol. Soc. 96 (12) (2015) 2059–2077, https://doi.org/10.1175/BAMS-D-14-00110.1.

[35] B.W. Silverman, Density Estimation for Statistics and Data Analysis, 26, CRC press, 1986, pp. 75–93.

[36] D. Behringer, Y. Xue, Evaluation of the global ocean data assimilation system at NCEP: the Pacific Ocean, in: Eighth Symposium on Integrated Observing and Assimilation Systems for Atmosphere, Oceans, and Land Surface, 2004.

[37] A. Sirois, J.W. Bottenheim, Use of backward trajectories to interpret the 5-year record of PAN and O₃ ambient air concentrations at Kejimkujik National Park, Nova Scotia, J. Geophys. Res. Atmos. 100 (D2) (1995) 2867–2881, https://doi.org/10.1029/94JD02951.

[38] L.L. Ashbaugh, W.C. Malm, W.Z. Sadeh, A residence time probability analysis of sulfur concentrations at Grand Canyon National Park, Atmos. Environ. 19 (8) (1985) 1263–1270, https://doi.org/10.1016/0004-6981(85)90256-2.

[39] J.H. Ryther, J.R. Hall, A.K. Pease, A. Bakun, M.M. Jones, Primary organic production in relation to the chemistry and hydrography of the Western Indian Ocean 1, Limnol. Oceanogr. 11 (3) (1966) 371–380, https://doi.org/10.4319/lo.1966.11.3.0371.

[40] M. Madhupratap, S.P. Kumar, P.M.A. Bhattathiri, M.D. Kumar, S. Raghukumar, K.K.C. Nair, N. Ramaiah, Mechanism of the biological response to winter cooling in the northeastern Arabian Sea, Nature 384 (6609) (1996) 549–552, https://doi.org/10.1038/384549a0.

[41] K. Chakraborty, V. Valsala, G.V.M. Gupta, V.V.S.S. Sarma, Dominant biological control over upwelling on pCO2 in sea east of Sri Lanka, J. Geophys. Res. Biogeosci. 123 (10) (2018) 3250–3261, https://doi.org/10.1029/2018JG004446.

[42] P.N. Vinayachandran, P. Chauhan, M. Mohan, S. Nayak, Biological response of the sea around Sri Lanka to summer monsoon, Geophys. Res. Lett. 31 (1) (2004), https://doi.org/10.1029/2003GL018533.

[43] C. Guieu, M. Al Azhar, O. Aumont, N. Mahowald, M. Levy, C. Éthé, Z. Lachkar, Major impact of dust deposition on the productivity of the Arabian Sea, Geophys. Res. Lett. 46 (12) (2019) 6736–6744, https://doi.org/10.1029/2019GL082770.

[44] S. Prasanna Kumar, P.M. Muraleedharan, T.G. Prasad, M. Gauns, N. Ramaiah, S.N. De Souza, S. Sardesai, M. Madhupratap, Why is the Bay of Bengal less productive during summer monsoon compared to the Arabian Sea?, 88–1, Geophys. Res. Lett. 29 (24) (2002), https://doi.org/10.1029/2002gl016013.

[45] G. Alory, G. Meyers, Warming of the upper equatorial Indian Ocean and changes in the heat budget (1960–99), J. Clim. 22 (1) (2009) 93–113, https://doi.org/10.1175/2008JCLI2330.1.

[46] M.K. Roxy, K. Ritika, P. Terray, S. Masson, The curious case of Indian Ocean warming, J. Clim. 27 (22) (2014) 8501–8509, https://doi.org/10.1175/JCLI-D-14-00471.1.

[47] S.K. Lee, W. Park, M.O. Baringer, A.L. Gordon, B. Huber, Y. Liu, Pacific origin of the abrupt increase in Indian Ocean heat content during the warming hiatus, Nat. Geosci. 8 (6) (2015) 445–449, https://doi.org/10.1038/ngeo2438.

[48] R.R. Rao, R. Sivakumar, Seasonal variability of sea surface salinity and salt budget of the mixed layer of the north Indian Ocean, 9–1, J. Geophys. Res. Oceans 108 (C1) (2003), https://doi.org/10.1029/2001JC000907.

[49] W. Han, J.P. McCreary Jr., Modeling salinity distributions in the Indian Ocean, J. Geophys. Res. Oceans 106 (C1) (2001) 859–877, https://doi.org/10.1029/2000JC000316.

[50] J.I. Goes, H. Tian, H.D.R. Gomes, O.R. Anderson, K. Al-Hashmi, S. deRada, H. Luo, L. Al-Kharusi, A. Al-Azri, D.G. Martinson, Ecosystem state change in the Arabian Sea fuelled by the recent loss of snow over the Himalayan-Tibetan plateau region, Sci. Rep. 10 (1) (2020) 7422, https://doi.org/10.1038/s41598-020-64360-2.

[51] B. Sridevi, S. Sabira, V.V.S.S. Sarma, Impact of ocean warming on net primary production in the northern Indian Ocean: role of aerosols and freshening of surface ocean, Environ. Sci. Pollut. Res. 30 (18) (2023) 53616–53634, https://doi.org/10.1007/s11356-023-26001-9.

[52] V.V.S.S. Sarma, D.N. Rao, G.R. Rajula, H.B. Dalabehera, K. Yadav, Organic nutrients support high primary production in the Bay of Bengal, Geophys. Res. Lett. 46 (12) (2019) 6706–6715, https://doi.org/10.1029/2019GL082262.

[53] P.D. Kumar, Y.S. Paul, K.R. Muraleedharan, V.S.N. Murty, P.N. Preenu, Comparison of long-term variability of Sea Surface temperature in the Arabian Sea and bay of Bengal, Reg. Stud. Mar. Sci. 3 (2016) 67–75, https://doi.org/10.1016/j.rsma.2015.05.004.

[54] A. Dai, T. Qian, K.E. Trenberth, J.D. Milliman, Changes in continental freshwater discharge from 1948 to 2004, J. Clim. 22 (10) (2009) 2773–2792, https://doi.org/10.1175/2008JCLI2592.1.

[55] M.K. Roxy, A. Modi, R. Murtugudde, V. Valsala, S. Panickal, S. Prasanna Kumar, M. Ravichandran, M. Vichi, M. Lévy, A reduction in marine primary productivity driven by rapid warming over the tropical Indian Ocean, Geophys. Res. Lett. 43 (2) (2016) 826–833, https://doi.org/10.1002/2015GL066979.